STUDY OF THE FORMATION MECHANISM OF URSA MINOR DWARF SPHEROIDAL GALAXY USING SUBARU/HSC WIDE FIELD DATA

佐藤, 恭輔 / SATO, Kyosuke

(出版者 / Publisher)
法政大学大学院理工学研究科
(雑誌名 / Journal or Publication Title)
法政大学大学院紀要. 理工学研究科編
(巻 / Volume)
65
(開始ページ / Start Page)
1
(終了ページ / End Page)
8
(発行年 / Year)
2024-03-24
(URL)
https://doi.org/10.15002/00030772

すばる望遠鏡/HSC で探るこぐま座矮小楕円体銀河の形成メカニズム

STUDY OF THE FORMATION MECHANISM OF URSA MINOR DWARF SPHEROIDAL GALAXY USING SUBARU/HSC WIDE FIELD DATA

佐藤恭輔
Kyosuke SATO
指導教員　小宮山裕　田中幹人　八木雅文

法政大学大学院理工学研究科システム理工学専攻前期課程

We investigate the star formation history of Ursa Minor dwarf spheroidal galaxy (UMi dSph) to address its formation mechanism from the analysis of color-magnitude diagram (CMD) using the g- and i-band wide field data observed by Hyper Suprime-Cam on the Subaru Telescope (Subaru/HSC). The method is based on the hybrid genetic algorithm (HGA) combining annealing and genetic algorithm to minimize a χ^2 merit function by comparing the observed CMD and synthetic CMD of simple stellar populations. The estimated Age-Metallicity Relations (AMRs) indicate that over 90% of star formation was completed before $z = 2$, and found the multiple populations suggested in a previous spectroscopic study which found both metal-rich population ($[\mathrm{Fe/H}] = -2.0$) and metal-poor population ($[\mathrm{Fe/H}] = -2.3$). We found that these populations formed simultaneously 12 Gyr ago. We also discovered the metal-poorer population ($[\mathrm{Fe/H}] = -2.7$) which was detected beyond 2 times the half-light radius, and the main sequence stars located beyond the tidal radius. These populations suggest the existence of a stellar halo of UMi dSph. From these results, it is suggested that UMi dSph should have experienced a few minor mergers in the past.

Key Words *: galaxies: dwarf – galaxies: evolution – galaxies: star formation – galaxies: interactions – Local Group*

1. Introduction

First billion years after the Big Bang, the first stars were born from primordial gases [1]. The material expelled from these stars by the supernovae included heavy elements and formed the first galaxies. Understanding the formation mechanism of the first galaxies is important to know our origin.

In the ΛCDM model, structures of the universe, such as galaxies, were formed in the density fluctuations of dark matter. The density fluctuation of the dark matter is enhanced with time, and the structure of the universe grows from the smaller scale (such as dwarf galaxies) to the larger scale (larger galaxies and galaxy clusters) to follow the fluctuation. This mechanism is called hierarchical clustering [2].

Dwarf galaxies are the smallest building blocks in the hierarchical clustering, and therefore they can be survivors of the first galaxies. The chemical composition of dwarf galaxies contains information on their first billion years. The reconstruction of the chemical evolutionary history allows us to understand star formation and metal enrichment processes in the early universe [3]. The Galactic dwarf galaxies are located within ~700 kpc from the Milky Way galaxy (MW) and provide the information of resolved stars observable from the large ground-based telescopes and the wide-field imager such as Subaru/HSC [42][43][44][45]. Thus, they are ideal targets for Near Field Cosmology [4]: a study of the early history of the Universe from the information of resolved stars.

The morphology, gas content, star formation history (SFH), and chemical abundance of Galactic dwarf galaxies vary with their distance from the Galaxy [5]. Dwarf Irregular Galaxies (dIrr) are mainly distributed beyond 300 kpc from the Galaxy and are weakly affected by tidal force from the Galaxy. They still contain gas and maintain star formation activity. On the other hand, Dwarf Spheroidal Galaxies (dSph) are located within ~300 kpc from the Galaxy and are affected by its strong tidal force. They have already lost gas and have stopped star formation. These facts indicate that there are varieties in the formation-evolution mechanisms of Galactic dwarf galaxies depending on their distance from the Galaxy [6].

Recent studies have found the substructures in dSphs. For example, the ring-like structure and satellites of dwarf galaxies were found in Sextans dSph [7], and the stellar halo-like structure was found in nine dwarfs including UMi dSph [8]. These substructures suggest that dwarf galaxies should have experienced accretions or mergers in the past [9]. Cosmological simulations also suggest that dwarf-dwarf mergers were not rare events [10], and some Galactic dwarf galaxies should have experienced mergers.

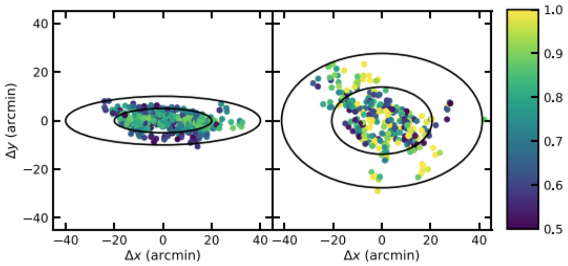

Figure 1: The spatial distribution of metal-rich with low-velocity dispersion (left) and metal-poor with high-velocity dispersion (right) populations of UMi dSph observed by the spectroscopic study using Keck/DEIMOS. The color shows the member probability [11].

UMi dSph is located 77 ± 4 kpc from the earth [18]. It is considered a candidate for "the first galaxy" because of its less-massive ($2.9 \times 10^5\ M_\odot$) [38] and low metallicity ($[\mathrm{Fe/H}] = -2.13$) [29] nature. Fig. 1 shows that UMi dSph exhibits multiple stellar populations, such as metal-rich with a low-velocity dispersion population in the center, and metal-poor with a high-velocity dispersion one in the outer regions [11][12]. The origin of the two-layer structure is still in debate. Several simulations have reproduced a two-layer structure separated at the center and outside, which is actively discussed [13][14][15][16].

Fig. 2 displays AMRs of some simulated dwarf galaxies with different formation mechanisms in the cosmological simulation. For example, in gas-rich mergers in the early universe, stars with low metallicities were bursty formed and dispersed by mergers, resulting in the extended distribution of low-metallicity stars [14]. Subsequently, star formation was thought to continue at the center of the galaxy for 5 Gyr by the slow accretion of gas with high metallicities. The model corresponds to Fig. 2:S-1 [13].

The two-layer structure can be explained by interaction with the intergalactic gas filament. In this scenario, when a dwarf galaxy interacts with an intergalactic gas filament. Stars with high metallicities were formed by the compression of the central gas due to ram pressure. Meanwhile, the outer gas was stripped by the ram pressure, and star formation was quenched. This model corresponds to Fig. 2:S-2. The area is painted with blue bands indicating the time of collision with the intergalactic gas filament.

Yet another explanation for the two-layer structure is the pericenter passage of the dwarf galaxy orbiting around the Galaxy [9]. The peak of star formation in the dwarf galaxy can also be explained by the explosive formation of metal-rich stars resulting from gas compression at the center during the pericenter passage. In Fig. 2:S-3, the dashed orange line indicates the distance from the MW, and the peak of star formation is consistent with the timing of the pericenter passage. The loss of most of the outer gas during the pericenter passage is thought to result in a multiple-layer structure of the galaxy.

In addition to the aforementioned scenarios, there are other scenarios for multiple-layer structures. They include the effect of supernova feedback and UV-background effects [16][17].

The differences between these scenarios are apparent in the AMRs (Fig. 2 middle). The gas-rich merger case (S-1) shows two peaks with the metal-poor population accounting for 90% of the total and the metal-rich population formed after the metal-poor one. In the case of the interaction with the intergalactic gas filaments (S-2), a metal-poor population was formed by 10 Gyr, and a young, metal-rich population was formed upon interaction. The case pericenter passage (S-3) shows the starburst in a short period with the timing of passage. Thus the shape of the AMRs differs depending on the events experienced by dwarf galaxies in the past. We thought that the formation mechanism of dwarf galaxies can be distinguished according to the shape of AMRs derived from the observational approach.

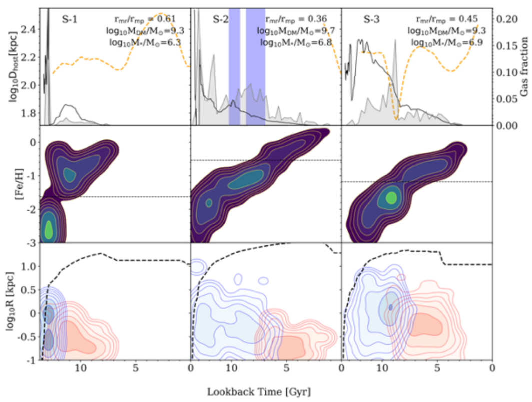

Figure 2 [13] : (top) Star formation history for dwarf-dwarf merger (S-1), interaction with intergalactic gas filament (S-2), and pericenter passage (S-3). Gray regions indicate star formation history, black lines indicate gas fraction, and orange dashed lines indicate distance from the MW. (middle) The AMR corresponds to each of the three scenarios. The color displays the Star Formation Rate (SFR), and the black dashed line is the boundary separating the populations with metallicities. (bottom) Age vs distance from the center. The contours show the number density of high(red) and low(blue) metallicity populations divided by the boundary shown in the middle panel.

In this study, we report observations of UMi dSph using the Subaru/HSC including regions further from its nominal tidal radius of 77.9±8.9 arcmin [18] and AMRs of UMi dSph derived from the observational approach. In addition, to search for the metallicity distribution varying with distance from the UMi dSph center, we derived AMRs for three regions divided by the radius of UMi dSph. Based on the estimated AMRs, we aim to constrain the formation and evolution history of UMi dSph.

2. Data

2. 1) Observation

Photometric observations were carried out on 2015 May 25(UTC) with the Subaru/HSC. Details are given in Table 1.

Table.1 Details of observation

Filter	g	i
Dates	2015/5/25	2015/5/25
Seeing	0".52~0".79	0".45~0".69
Exposuretime	10 × 180 sec	20 × 180 sec

2. 2) Reduction and measurements

We reduced the HSC data and measured the photometric properties of detected objects using the HSCpipe 8.5.3 [19]. HSCpipe, firstly, carried out Bias subtraction, Dark subtraction, and Flat fielding for each CCD in single-visit processing. The "visit" is a complete set of data from 112 CCDs obtained with one exposure. Secondly, the photometric zero point was estimated by comparing bright objects with the Pan-STARRS1 catalog [20] for each visit [39]. The objects are used for Point Spread Function (PSF) measurement. After that, cosmic rays were removed. Next, sky subtraction was conducted, and the world coordinate system (WCS) and photometric zero points were determined for each CCD. Using the WCS, the stacked image was created by combining multiple visits in each band. After the stacking, three types of photometry were conducted. In this work, we didn't use Kron photometry and used the CModel photometry and PSF photometry. The CModel photometry is the optimized way for a photometry of galaxies to fit by a combination of Sérsic profiles [21] with Sérsic indices n = 1 and 4 to the object [19]. The difference between PSF and CModel photometry allows us to separate stars from galaxies. In this study, ideally, we made and used a catalog of stars (though it is not a perfect star-only catalog).

Next, we carried out the reddening correction to correct the extinction (= absorption + scattering) caused by the interstellar dust in MW in the following way. We estimated the value of $E(B-V)$ for each object from the interstellar dust map of Schlegel et al. (1998) [22]. We also derived the spectrum of F5V-type stars generated by Castelli and Kurucz (2003) [23], and multiplied the system throughput (i.e., atmospheric extinction, throughput of optics, transmittance of filters, and quantum efficiency of CCD). The result allowed us to obtain the effective wavelength in each band when a source is observed with Subaru/HSC. Finally, we calculated extinction values for each object in each of the g- and i-bands from the interstellar extinction curves of Fitzpatrick (1999) [24]. The mean values in the g- and i-band were 0.09 mag and 0.04 mag, respectively.

2. 3) Completeness

When observing with a telescope, the detection rate of faint objects is gradually reduced as it goes to a fainter magnitude. In addition, when observing crowded regions such as a globular cluster, blending of point sources can reduce the detection rate. These effects cause the underestimation of the number of fainter stars in some systems. Therefore, we estimated the detection completeness and then inversely weighted to the observed CMD to reproduce the actual number density of stars in the UMi dSph.

To derive the detection completeness of photometric data, we ran the artificial star detection test [25]. In this test, we added fake point sources to the stacked image. We used the PSF estimated in each patch, (2800×2800 pixel^2 sub-region of the stacked image). We then generated artificial stars from these PSFs at every 0.5 magnitudes from 16 to 28 mag and added them to stacked images at every 60×60 pixel^2. Fig. 3 displays the detection completeness for each band and that overlayed on the CMD. Fig. 4 displays the detection completeness map.

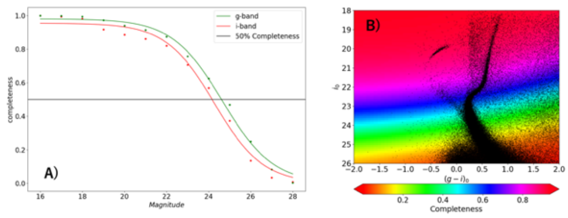

Figure 3(A) Detection completeness of g- and i-band. Colored solid lines correspond to the results of curve approximation [26], and the black solid line shows 50% completeness. (B) The detection completeness is indicated by background color in the CMD.

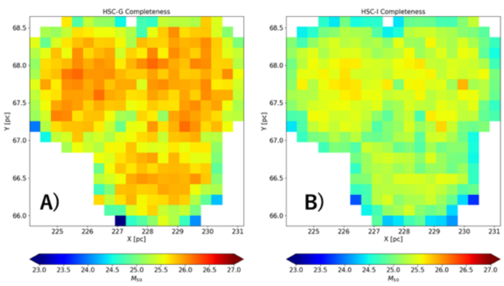

Figure 4: g- (A) and i-bands (B) map of detection completeness. Color show the magnitude at 50% detection completeness.

2. 4) CMD of UMi dSph

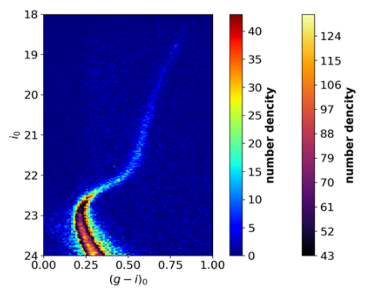

Figure 5: The CMD of the UMi dSph after the correction of the detection completeness and reddening. The left color bar shows the low number density, and the right one is the high number density.

Fig. 5 is the CMD of the UMi dSph after the correction of the detection completeness and reddening. The subscript 0 means the magnitude or the color after extinction correction (or the value not affected by the Galactic extinction) throughout this work. Various evolutionary stages of UMi dSph stars are observed in the plot. Red Giant Brunch (RGB) stars ($i < 22$) are highly sensitive to stellar metal abundance and are useful for estimating the metallicity distribution of the galaxy. The Main Sequence Turn Off (MSTO) stars at $22 < i < 23$ mag are good trackers of age. The RGB and MSTO stars are important for estimating the age and metallicity. On the other hand, the plot includes Galactic halo stars (thin and uniformly distributed at $g - i > 0.4$). The fainter magnitude than the range of this plot, $i = 25\sim26$ mag, background galaxies also contaminate in $(g - i)\_0 < 0.5$, which were classified as point sources due to their large distance.

3. Analysis

3. 1) Half-light radius of UMi dSph

The half-light radius is defined as the radius in which half of the total luminosity of a galaxy is included. The Markov Chain Monte Carlo (MCMC) method was used to perform fitting based on the log-likelihood described as equation (5) for the spatial distribution of UMi dSph. The density profile was defined in equations (1), (2),(3), and (4) [26].

$$\rho_{dwarf}(r) = \frac{1.68^2}{2\pi r_h^2 (1-e)} N^* \exp\left(-\frac{1.68r}{r_h}\right), \qquad (1)$$

where $\rho_{dwarf}(r)$ is the assumed radial density profile of dwarf galaxies, e is the ellipticity which is defined by the major (a) and minor (b) axes as $e = 1 - b/a$, r_h is the half-light radius, N^* is the number of UMi member stars, and r is the elliptical radius defined in equation (2)

$$r = \left(\left(\frac{1}{1-e}\left((x-x_0)\cos\theta - (y-y_0)\sin\theta\right)\right)^2 + \left((x-x_0)\sin\theta - (y-y_0)\cos\theta\right)^2\right)^{\frac{1}{2}}, \qquad (2)$$

where x_0 and y_0 are the center coordinate of the galaxy and θ is the position angle. To account for the background and foreground contamination, we define the background density as

$$\rho_{background} = \frac{\left(N_{tot} - \int \rho_{dwarf} dA\right)}{\int dA}, \qquad (3)$$

where N_{tot} is the number of UMi member stars plus contaminations, $\rho_{model}(r)$ is a radial density profile defined as

$$\rho_{model}(r) = \rho_{dwarf}(r) + \rho_{background}. \qquad (4)$$

The log-likelihood P_{tot} for estimation is defined as

$$P_{tot} = \Sigma_k \log\left(\frac{\rho_{model}(d_k|\mathcal{P})}{\int \rho_{model} dA}\right), \qquad (5)$$

where d_k is the coordinate of each object in the catalog, and A is the area covered by the catalog, and $\mathcal{P}$ is a set of parameters. In the MCMC analysis, x_0, y_0, r_h, e, θ, N^* were estimated. The fitting obtained the center coordinate of $(\mathrm{RA}, \mathrm{Dec})(\mathrm{J2000}) = (227.285 \pm 0.004\ [\mathrm{deg}], +67.212 \pm 0.002\ [\mathrm{deg}])$, the half-light radius of 17.4 ± 0.1 arcmin, the position angle of 50.40 deg, and the ellipticity of $0.46^{+0.00}_{-0.01}$. The result is displayed in Fig. 6.

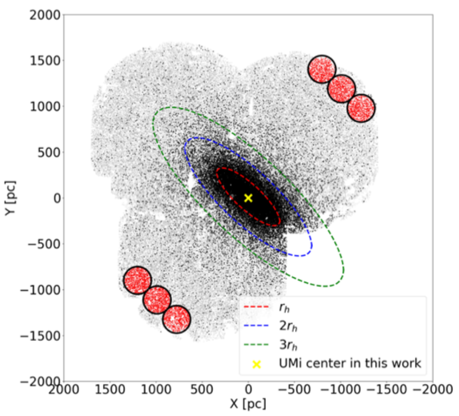

Figure 6: The spatial distribution of UMi dSph with objects shown as black points. The ellipse of the half-light elliptical radius is shown as a red dashed line. The center coordinate (yellow cross) of UMi dSph, is $(\mathrm{RA}, \mathrm{Dec})(J2000) = (227.285\ [\mathrm{deg}], +67.212\ [\mathrm{deg}])$. Red points encircled by black lines are set as control fields. Their radius is 150 pc.

3. 2) Reduction of contamination

As described in Sec. 2.3, the UMi dSph stellar catalog contains contaminations from foreground stars and background galaxies. To remove them, we, firstly, tried to use six regions shown in Fig.6 as a control field, assuming that no UMi dSph member stars are found in these regions. This control field is located more than $7 \times r_h$, where is far beyond the predicted tidal radius of $50'.6$ [40]. Fig. 7 displays the CMD of the control field. The sequence corresponding to the main-sequence (MS) stars of UMi dSph is visible at 23~25 mag along the isochrone. Thus, we failed to use these regions as the control field, because it includes UMi member stars. Therefore, in this study, we set the box area of $(240 \leq \mathrm{RA} \leq 246, +42.5 \leq \mathrm{Dec} \leq +44.5)$, where is at the same Galactic latitude of UMi dSph, for the control field, and obtained photometric catalog from wide-field data of the Hyper Suprime-Cam Subaru Strategic Program (HSC/SSP) DR3[41]. More details are given in Sec. 5.2.

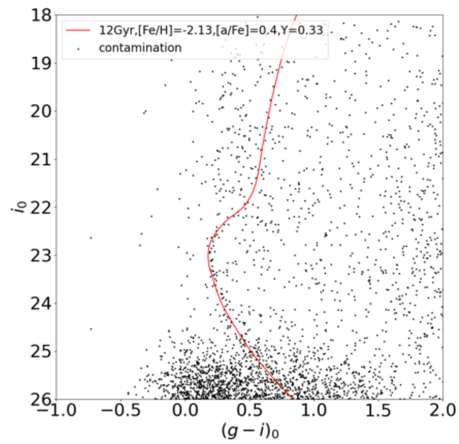

Figure 7: CMD made from the sum of the control field. The red line is the Dartmouth isochrone [30] corresponding to typical ages [28] and metallicities [29] of UMi dSph.

3. 3) Simple stellar population (SSP)

The SSP is consistent with a stellar system that has a single population composed of a specific age and chemical abundance. The isochrone and Initial Mass Function (IMF) were used to create the SSP. The isochrone is the line connecting the positions of stars of the same age and chemical composition with different masses on the CMD, which are calculated by the theory of stellar evolution. The IMF is a mass distribution of stars born from a single molecular cloud.

The red solid line in Fig. 7 is the Dartmouth isochrone [30], with $[\mathrm{Fe/H}] = -2.13$ and age of 12Gyr . Various institutes provide isochrones. They have their own unique characteristics in the calculation of stellar evolution. The previous study by Mori (2023) [33] constructed an algorithm that utilizes the Dartmouth isochrone [30]. However, the lower limit of metallicity $[\mathrm{Fe/H}] > -2.5$ of the Dartmouth isochrone was insufficient for the analysis of low-metallicity dwarf galaxies.

In this study, we use A Bag of Stellar Tracks and Isochrones (BaSTI) [31], which covers the metallicity range of dwarf galaxies, $[\mathrm{Fe/H}] > -3.2$. The strength of BaSTI is that in contrast to Dartmouth isochrone, the evolution of horizontal branch stars and asymptotic giant branch stars is also calculated. The α abundance and helium fraction of BaSTI were set to $[\alpha/\mathrm{Fe}] = 0.4$, and $Y = 0.275$, respectively. To generate the CMD of SSP, we created a stellar mass and magnitude function from the isochrone and inserted the IMF into the function. We adopted the Kroupa IMF [32]. We also considered the effect of binaries, which is important for reproducing the CMD at the main sequence. Since the flux of binaries is a sum of fluxes of primary and companion stars, binaries show more extended distribution on the CMD than single stars. The binary fraction and mass ratio of the stellar system were assumed to be 0.5 and uniform distribution, respectively. Finally, we add an artificial noise to the magnitudes of each star to represent the photometric error in each band. We also convert the absolute magnitude to the apparent magnitude using the distance modulus of $\mathrm{m} - \mathrm{M} = 19.16$. This distance modulus was estimated from this study by comparing the isochrone of the typical parameter of UMi dSph shown in Fig. 7. Figure 8 shows an example of the resulting CMD of an SSP.

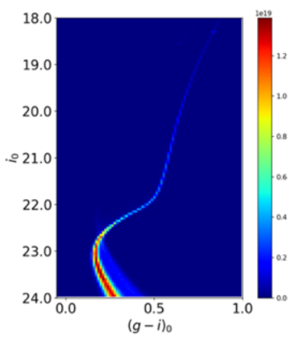

Figure 8: SSP created from BaSTI, with age set to 12 Gyr, α abundance to $[\alpha/\mathrm{Fe}] = 0.4$, metallicity to $[\mathrm{Fe/H}] = -2.0$, helium fraction to $Y = 0.275$, binary fraction 0.5 , and distant modulus $\mathrm{m} - \mathrm{M} = 19.16$.

3. 4) Hybrid Genetic Algorithm for Age Metal Relation

For the estimation of the AMR of UMi dSph, we improved the HGA developed in Mori's master thesis (2023) [33][34]. HGA is a combination of the genetic algorithm and the annealing. The genetic algorithm (GA) models the mechanism of biological evolution and is suitable for searching for globally optimal solutions through processes such as crossover and mutation. Annealing is a local search optimization technique that was inspired by metallurgical engineering. It accepts if solutions become worse, with a probability that depends on the number of trials. In HGA, the advantages of GA and annealing.

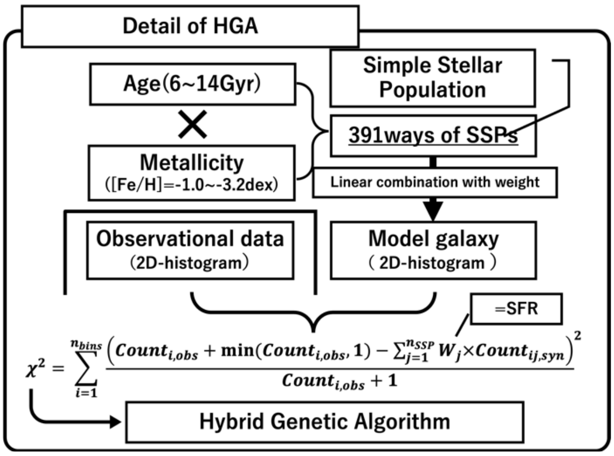

Figure 9: The procedure of the AMR estimation by HGA

In HGA, we, firstly, generated 391 SSPs (6~14 Gyr with 0.5 Gyr interval, and $-3.2 \leq [\mathrm{Fe/H}] \leq -1.0$ with 0.1 dex interval). Secondly, the CMD of a model galaxy was created by the linear combination of weighted SSPs. These weights correspond to the SFR of each population, and they were estimated by HGA. In Fig. 9, the procedure of HGA is displayed. Both CMDs of the observed and model galaxies were displayed in the left panels of Fig. 10 as 2D histograms. To find the best combination of weights for the model galaxy, we used the chi-square value defined as equation (6) as a merit function.

$$\chi^2 = \sum_{i=1}^{n_{bins}} \frac{\left(Count_{i,obs} + \min(Count_{i,obs}, 1) - \sum_{j=1}^{n_{SSP}} W_j \times Count_{ij,syn}\right)^2}{Count_{i,obs} + 1} , \quad (6)$$

where $Count_{i,obs}$ indicates the number of stars in each bin of the 2D histogram of the observed CMD, W_j is the

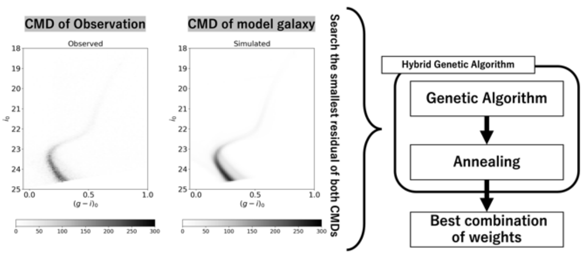

Figure 10: Conceptual diagram of the steps of HGA. The left panels show the CMDs of the observed and model galaxy.

weight of each SSP (corresponding to the SFR), $Count_{ij,syn}$ is the s number of stars in each bin of the 2D histogram of the CMD created from the SSP.

This chi-square value used in the HGA is based on Mighell et al. (1999) [35], and the value was obtained by comparing the two CMDs.

3. 5) Verification of the accuracy of algorithms using artificial galaxies

This section evaluated the accuracy of the peak reproducibility in the AMR and the accuracy of our algorithm using a mock galaxy with a given AMR [36]. For evaluation, we created the CMD of the mock galaxy by linearly combining 391 SSPs with artificially set AMRs as weights. The AMR is shown in Fig. 11A. The input AMR includes two star formations that occurred simultaneously 13 Gyr ago, with metallicities of [Fe/H] $= -2.0$ and -2.5. We modeled the extended star formation and metallicity distribution of UMi dSph as a 2-dimensional Gaussian distribution with an age dispersion (σ_{age}) of 0.05 Gyr and a metallicity dispersion (σ_{metal}) of 0.01 dex.

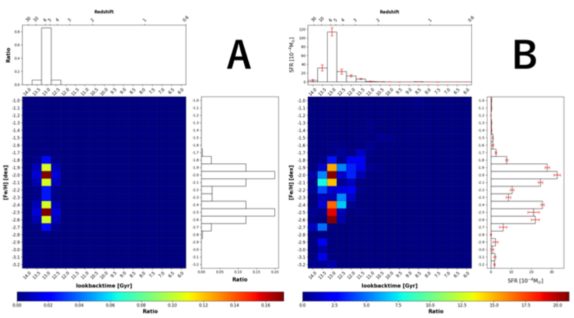

Figure 11: (A) The AMR was set for the mock galaxy, which has two populations with simultaneous star formation 13 Gyr ago, and a difference in metallicity of 0.5 dex. (B) The estimated AMR from the CMD of the mock galaxy using HGA. In both A and B, the right-side histograms are the metallicity distribution. The top-side histograms are SFH. The color indicates the weights of each corresponding SSP.

Furthermore, we overlaid the CMD of contamination (Secs. 3.2 and 5.2) onto the CMD of the mock galaxy. The input parameters required to make simple stellar populations, such as α abundance, helium fraction, distance modules, binary fraction, mass ratio distribution, and IMF, were the same as those used in Sec. 3.3. Fig. 12A displays the CMD of the mock galaxy.

The derived AMR is displayed in Fig. 11B. The metallicity distribution is in the right-side histogram. The mean values of each population were consistent with the input AMR, but the SFRs of the metal-poor population were underestimated compared to the metal-rich one. On the other hand, the estimation of age was accurate.

To verify the underestimation of the metal-poor population, we created CMDs of mock galaxies of a single population of different metallicities. From these CMDs, we estimated the metallicity distribution and fitted the Gaussian distribution for it to estimate the mean value and dispersion. Fig.13 shows the comparison of the results of the Gaussian fit and the

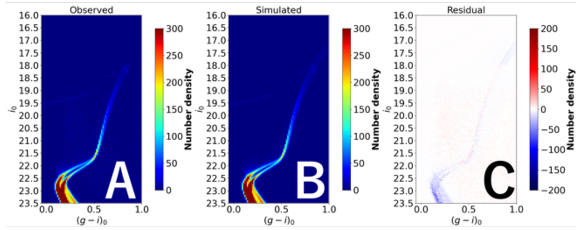

Figure 12: The CMD of the mock galaxy (A). The synthetic CMD was estimated by HGA (B). The difference between both (C). For all CMDs, bin size set for 0.075×0.025 mag.

input parameter. The dispersion of the metallicity distribution tends to increase around [Fe/H] $= -2.5$. This trend is thought to be the cause of underestimation of SFRs. In addition, the mean value of each Gaussian didn't overlap with 1 sigma ranges of neighbors, except [Fe/H] = -3.0. This means that HGA can distinguish two populations different by 0.25 dex in metallicity. Thus, HGA is working reasonably to disentangle different populations on AMR. These results show the effectiveness of HGA in the distinction of multiple populations in dwarf galaxies.

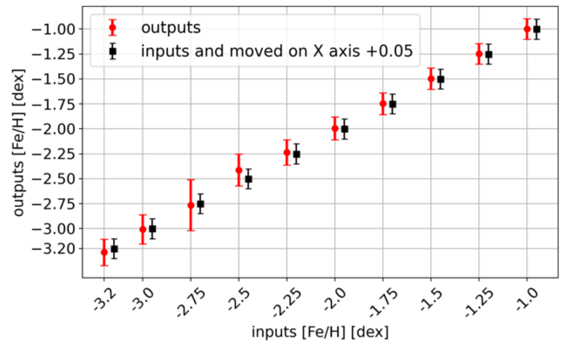

Figure 13: The comparison of metallicity between input (black points and offset by 0.05 to x+) and estimated value (red points) of single-population mock galaxies.

4. Result

In this section, we divided the whole data region into three groups (Fig. 6) according to the (elliptical) distance from UMi center and obtained AMRs for each group. We set the 3 regions as $r \leq r_h, r_h < r \leq 2r_h$, and $2r_h < r \leq 3r_h$ for estimations. We applied the HGA to these CMDs.

Figs. 14, 16A, and 16B display the AMR of three regions. The metallicity distributions and the SFH are displayed in right-side and top-side histograms, respectively. We carried out 100 times re-sampling bootstrapping, and the error shown in the histogram is estimated from the rms of the 100 trials. According to Fig. 14, the star formation peak was found to be 12.5 Gyr ago, and over 90% of stars were formed by $z \sim 2$. Fig. 15A displays the CMD of the UMi dSph of $r \leq r_h$, Fig. 15B is the synthetic CMD derived from HGA, and Fig. 15C is the difference between Fig. 15A and Fig.

15B.

According to Fig. 16 A and B, the outer region of UMi dSph, first, formed very metal-poor stars (VMPs) with [Fe/H] ≤ -2.5 between 14 Gyr and 13.5 Gyr ago which corresponds to the first 0.5 Gyr after the Big Bang.

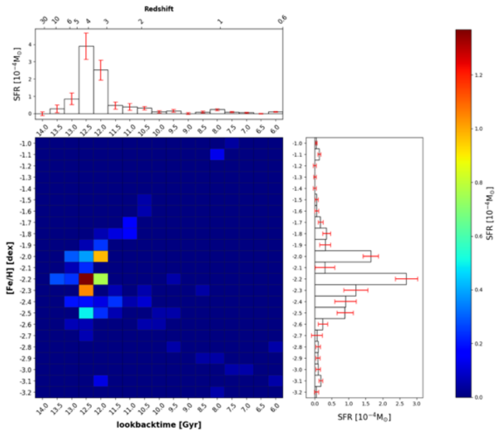

Figure. 14: The AMR was estimated from the region of an ellipse $r \leq r_h$. The color shows the SFR for each population. For estimation, we conducted the 100 times re-sampling bootstrapping, and the errors plotted in both metallicity distribution and SFH were estimated by the 1σ from it.

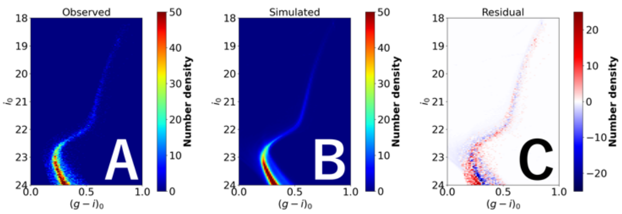

Figure 15: The CMD of the UMi dSph (A) of $r \leq r_h$ region. The synthetic CMD estimated by HGA (B). The difference between both (C). For all CMDs, bin size set for 0.075×0.025 mag.

In $r_h < r < 2r_h$ region, metal-poor populations are more abundant than in the inner $r \leq r_h$ region. In addition. in $2r_h < r \leq 3r_h$ region, the metal-poorer population ([Fe/H] ≤ -2.7) was discovered, and this metallicity is consistent with that found in the previous spectroscopic study [27].

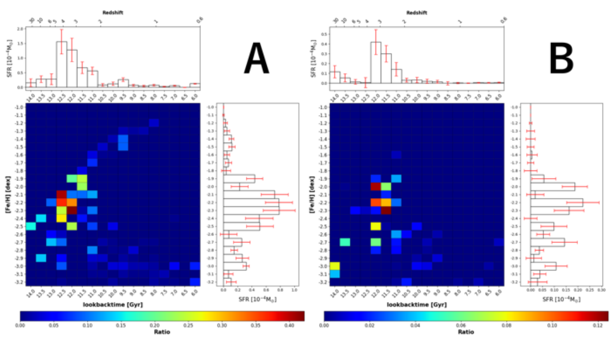

Figure 16: The AMR was estimated from the region of ellipse rings $r_h < r \leq 2r_h$ (A) and $2r_h < r \leq 3r_h$(B).

5. Discussion

5. 1) The comparison of the results of cosmological simulation

The estimated AMRs of UMi dSph (Figs. 14 and 16) resemble the AMR of the dwarf-dwarf merger model derived from the cosmological simulation (Fig. 2:S-1). This similarity suggests that UMi dSph would have been made by the merger of two different molecular clouds, which were affected by the different first stars for each merged in the first universe. Additionally, the detection of the metal-poorer population in $2r_h < r$ suggests that different molecular clouds would have fallen onto the UMi dSph.

5. 2) Effect of contamination

In this study, we used the box area of $(240 \leq \mathrm{RA} \leq 246, +42.5 \leq \mathrm{Dec} \leq +44.5)$ in the wide-field data of the HSC/SSP to correct for the contamination caused by foreground stars. This area is at the same Galactic latitude of UMi dSph, and therefore, we assume this area has a comparable number density of foreground stars. However, the contamination was not continuously spread over the CMD due to the small number of stars in the outer regions. Thus, we failed to reproduce the distribution of contamination on synthetic CMD. To obtain a more accurate estimation of AMR, it is necessary to reduce the effects of contaminations. Stellar motion obtained from Gaia data may be considered for removing contamination.

5. 3) More extended structure of UMi dSph.

In Sec. 3.2, we discovered the MS stars in the region more than 7 times of half-light radius away. These regions are located beyond the tidal radius. The extended MS distribution suggests that the UMi dSph may be more extended than previously thought. Recently, some spectroscopic studies found bright stars that are members of UMi dSph [8][27] located beyond the tidal radius. Sestito et al. (2023) found 5 member RGB stars and their metallicity is lower than that of the ones found before. Some of their metallicity was consistent with our results ([Fe/H] $= -2.7$) found in $2r_h < r \leq 3r_h$ region.

MS stars are more numerous than brighter RGB stars found in previous studies. The larger number of stars allows us to study the distribution and other parameters of metal-poor populations in more detail. We plan to observe more outer regions of UMi dSph using Subaru/HSC.

6. Conclusion

We simultaneously derived the SFH and metallicity distribution of UMi dSph from the Subaru/HSC wide-field data. For estimation, we divided the data into three areas (Fig. 6) according to the (elliptical) distance from UMi center and obtained AMRs for each group. The results showed that over 90% of star formation ended by $z{\sim}2$. We found two populations discovered in previous work [11] with simultaneous star formation.

This result was consistent with the results from the cosmological simulation which re-produced the dwarf-dwarf merger. Additionally, the metal-poor ([Fe/H] ≈ -2.2) population was found to be more abundant than the metal-rich population ([Fe/H] ≈ -2.0). The detection of the extended distribution of MS stars and the metal-poorer population beyond the tidal radius suggests the existence of a structure like stellar halo.

We also established a reasonable algorithm, HGA, to estimate age and metallicity from observed CMD. We examined the accuracy of the estimation using the CMD of mock galaxies and concluded that our algorithm was reasonable.

References

[1] Palla, F. et al: PRIMORDIAL STAR FORMATION: THE ROLE OF MOLECULAR HYDROGEN, ApJ, 271, 632, 1983

[2] White & Frenk: GALAXY FORMATION THROUGH HIERARCHICAL CLUSTERING, ApJ, 379, 52, 1991

[3] Anna Frebel & John E. Norris: Near-Field Cosmology with Metal-Poor Stars, ARA&A, 53, 631, 2015

[4] Freeman & Bland-Hawthorn : The New Galaxy: Signatures of its Formation ARA&A, 40, 487, 2002

[5] Grebel, E. K.: Evolutionary Histories of Dwarf Galaxies in the Local Group, IAUS, 192, 17, 1999

[6] Tolstoy et al: Star-Formation Histories, Abundances, and Kinematics of Dwarf Galaxies in the Local Group, ARA&A, 47, 371, 2009

[7] Cicuéndez & Battaglia: Appearances can be deceiving: clear signs of accretion in the seemingly ordinary Sextans dSph, MNRAS, 480, 251, 2018

[8] Jensen et al: Small-scale stellar haloes: detecting low surface brightness features in the outskirts of Milky Way dwarf satellites, MNRAS, 527, 4209, 2024

[9] del Pino et al: Rotating stellar populations in the Fornax dSph galaxy, MNRAS, 465, 3708, 2017

[10] Deason, Wetzel & Garrison-Kimmel: Satellite Dwarf Galaxies in a Hierarchical Universe: The Prevalence of Dwarf-Dwarf Major Mergers, ApJ, 794, 11, 2014

[11] Pace et al: Multiple chemodynamic stellar populations of the Ursa Minor dwarf spheroidal galaxy, MNRAS, 495, 3022, 2020

[12] Hayashi et al: Dark halo structure in the Carina dwarf spheroidal galaxy: joint analysis of multiple stellar components, MNRAS, 481, 250, 2018

[13] Genina et al: The distinct stellar metallicity populations of simulated Local Group dwarfs, MNRAS, 488, 2312, 2019

[14] Benítez-Llambay et al: Mergers and the outside-in formation of dwarf spheroidals, MNRAS, 456, 1185, 2016

[15] Wright et al: Reignition of star formation in dwarf galaxies, MNRAS, 482, 1176, 2019

[16] El-Badry et al: BREATHING FIRE: HOW STELLAR FEEDBACK DRIVES RADIAL MIGRATION, RAPID SIZE FLUCTUATIONS, AND POPULATION GRADIENTS IN LOW-MASS GALAXIES, ApJ, 820, 131, 2016

[17] Hidalgo et al: The ACS LCID Project. IX. Imprints of the Early Universe in the Radial Variation of the Star Formation History of Dwarf Galaxies, ApJ, 778, 103, 2013

[18] Wolf et al: Accurate masses for dispersion-supported galaxies, MNRAS, 406, 1220, 2010

[19] Bosch, J. et al: The Hyper Suprime-Cam software pipeline PASJ, 70, 5, 2017

[20] Chambers et al: The Pan-STARRS1 Surveys, arXiv:1612.05560, 2016

[21] Sérsic: Influence of the atmospheric and instrumental dispersion on the brightness distribution in a galaxy, BAAA, 6, 41, 1963

[22] Schlegel, D. et al: MAPS OF DUST INFRARED EMISSION FOR USE IN ESTIMATION OF REDDENING AND COSMIC MICROWAVE BACKGROUND RADIATION FOREGROUNDS, ApJ, 500, 525, 1998

[23] Castelli & Kurucz: New Grids of ATLAS9 Model Atmospheres, IAUS, 210, A20, 2003

[24] Fitzpatrick: Correcting for the Effects of Interstellar Extinction, PASP, 111, 63, 1999

[25] Ogami et al. The structure of the stellar halo of the Andromeda galaxy explored with the NB515 for Subaru/HSC. I.: New Insights on the stellar halo up to 120 kpc, arXiv:2401.00668, 2024

[26] Martin et al: The PAndAS View of the Andromeda Satellite System. II. Detailed Properties of 23 M31 Dwarf Spheroidal Galaxies, ApJ, 833, 67, 2016

[27] Sestito et al: The extended "stellar halo" of the Ursa Minor dwarf galaxy, MNRAS, 525, 2875, 2023

[28] Kleyna et al: A DYNAMICAL FOSSIL IN THE URSA MINOR DWARF SPHEROIDAL GALAXY, ApJ, 588, L21, 2003

[29] Kirby et al: Multi-element Abundance Measurements from Medium-resolution Spectra. III. Metallicity Distributions of Milky Way Dwarf Satellite Galaxies, ApJ, 727, 78, 2011

[30] Dotter et al. : The Dartmouth Stellar Evolution Database, ApJS, 178, 89, 2008

[31] Pietrinferni et al: UPDATED BASTI STELLAR EVOLUTION MODELS AND ISOCHRONES: II. α−ENHANCED CALCULATIONS, ApJ, 908, 102, 2021

[32] Kroupa: On the variation of the initial mass function, MNRAS, 322, 231, 2001

[33] 森 林太郎: すばる望遠鏡/Hyper Suprime-Cam で探るりゅう座矮小銀河の星形成史, 法政大学修士論文, 2023

[34] Cignoni et al: Hubble Tarantula Treasury Project. II. The Star-formation History of the Starburst Region NGC 2070 in 30 Doradus, ApJ, 811, 76, 2015

[35] Mighell, K.J: Parameter Estimation in Astronomy with Poisson-distributed Data. I. The χ_γ^2 Statistic, ApJ, 518, 380, 1999

[36] Aparicio & Hidalgo: IAC-pop: Finding the Star Formation History of Resolved Galaxies, AJ, 138, 558, 2009

[37] Hidalgo et al: The ACS LCID Project. V. The Star Formation History of the Dwarf Galaxy LGS-3: Clues to Cosmic Reionization and Feedback, ApJ, 730, 14, 2011

[38] McConnachie: The Observed Properties of Dwarf Galaxies in and around the Local Group, AJ, 144, 4, 2012

[39] Song et al: Characterization and photometric performance of the Hyper Suprime-Cam Software Pipeline, PASJ, 70S, 6, 2018

[40] Palma et al: Exploring Halo Substructure with Giant Stars. IV. The Extended Structure of the Ursa Minor Dwarf Spheroidal Galaxy, AJ, 125, 1352, 2003

[41] Aihara et al: Third data release of the Hyper Suprime-Cam Subaru Strategic Program, PASJ, 74, 247, 2022

[42] Miyazaki, S. et al: Hyper Suprime-Cam: System design and verification of image quality, PASJ, 70, S1, 2018

[43] Komiyama, Y. et al: Hyper Suprime-Cam: Camera dewar design, PASJ, 70, S2, 2018

[44] Kawanomoto, S. et al: Hyper Suprime-Cam: Filters, PASJ, 70, 66, 2018

[45] Furusawa, H. et al: The on-site quality-assurance system for Hyper Suprime-Cam: OSQAH, PASJ, 70, S3, 2018